

# Bioinspiration & Biomimetics



## PAPER

# A variable stiffness gripper based on differential drive particle jamming

RECEIVED  
21 November 2018

REVISED  
28 January 2019

ACCEPTED FOR PUBLICATION  
6 February 2019

PUBLISHED  
8 March 2019

Pei Jiang<sup>1</sup>, Yandong Yang<sup>1</sup>, Michael Z Q Chen<sup>2</sup> and Yonghua Chen<sup>3</sup>

<sup>1</sup> College of Mechanical Engineering, Chongqing University, Chongqing 400030, People's Republic of China

<sup>2</sup> School of Automation, Nanjing University of Science and Technology, Nanjing, Jiangsu 210094, People's Republic of China

<sup>3</sup> Department of Mechanical Engineering, The University of Hong Kong, Hong Kong 999077, People's Republic of China

E-mail: [Peijiang@cqu.edu.cn](mailto:Peijiang@cqu.edu.cn) (Pei Jiang) and [mzqchen@outlook.com](mailto:mzqchen@outlook.com) (Michael Z Q Chen)

**Keywords:** particle jamming, differential drive particle jamming, fiber reinforcement, stiffness variation, variable stiffness gripper

Supplementary material for this article is available [online](#)

## Abstract

Compared with rigid grippers, soft grippers show fantastic adaptability and flexibility in grasping irregularly shaped and fragile objects. However, the low stiffness of the soft actuator limits the scope of applications. Particle jamming has emerged as an important method to adjust the stiffness of soft grippers. This paper proposes a novel particle jamming mechanism based on the differential pressure drive. With the differential drive particle jamming mechanism, a soft actuator is designed, which is characterized by a dual-deformable chamber structure in which one chamber is filled with particles. The simultaneous inflation of the two chambers will result in the bending behavior without significant stiffening. However, if the air chamber is pressurized with a larger pressure, the differential pressure will cause the particles inside the particle chamber to jam each other, which increases the stiffness of the actuator significantly. Thus, the differential drive particle jamming mechanism can achieve the independent control of the stiffness and the bending angle. Both theoretical and experimental studies in this area have shown that the gripper based on the differential drive particle jamming mechanism can stiffen itself effectively, and achieve the independent control of the stiffness and the bending angle, which can be adopted in applications where both high stiffness and dexterity are required.

## 1. Introduction

In recent years, an increasing number of robots have been adopted in the human-robot interactive environment. Realizing compliance has attracted increasing attention in robotic research for safety concerns. Thus, soft robots emerged, which can achieve high compliance, adaptiveness and safety by preprogramming complex motions into flexible structures. The soft gripper is one of the most promising fields of soft robots due to inexpensive and convenient fabrication. Compared with traditional rigid hands grasping and manipulating target objects with hard contacts, soft grippers can grasp delicate objects with soft contacts, and the adaptability of soft grippers to the object shapes could ease the control of the grasping process.

A large number of soft grippers or actuators have been reported in the literature in recent years. In general, the robots or actuators made of elastomer mat-

erial are powered by fluidic pressures (pneumatics or hydraulics) [1–3], tendons [4, 5], electric/magnetic forces [6, 7], and chemical reactions [8]. The soft actuator with fluidic actuation shows a great application potential due to its light weight, low material cost and simple fabrication. The pneumatic artificial muscle was first developed, which produces a linear extension with pressurization, and has been adopted in rehabilitation devices. It is also used as an actuator in robots, including industrial robots, which is designed to cooperate with human beings [9]. However, it is difficult for the pneumatic artificial muscle to create bending motions. Thus, soft-bending actuators were proposed to achieve expansion and bending motions simultaneously. Bobak Mosadegh *et al* proposed a pneumatic networks bending actuator in [10], where bending motions can be achieved as the embedded chambers are pressurized.

In addition, a fiber-reinforced bending actuator was developed by Bishop-Moser [11, 12]. Compared with the pneumatic network bending actuator, the soft

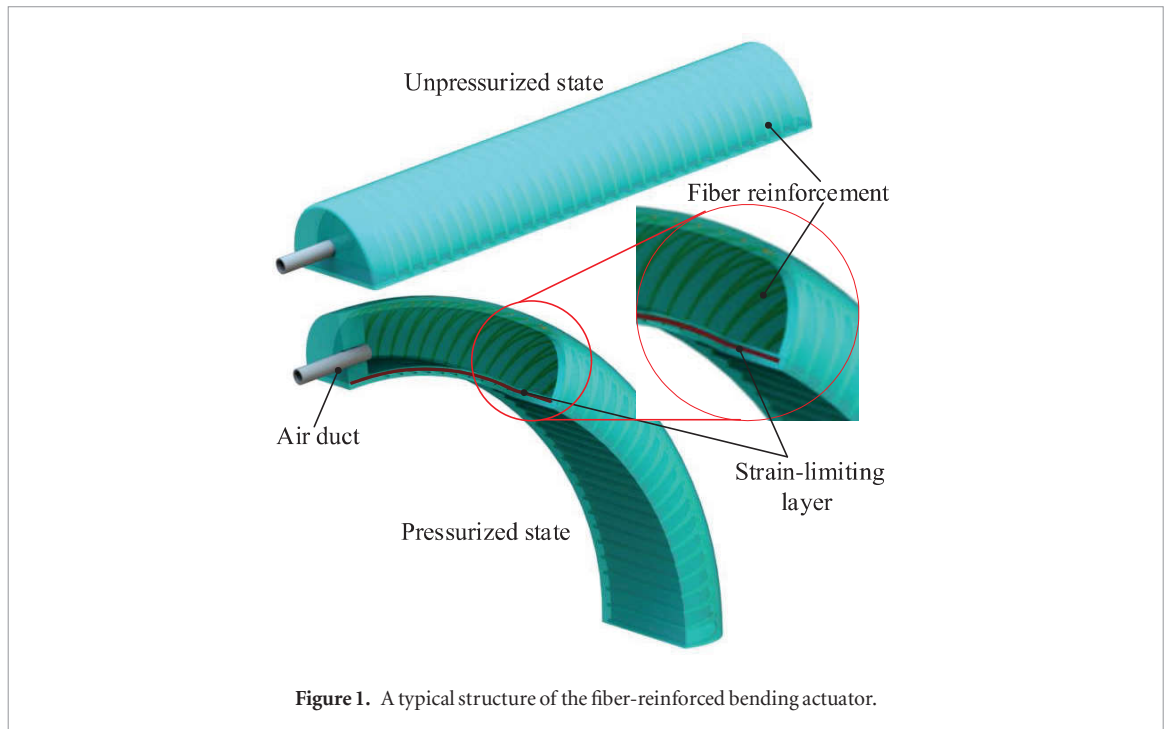


**Figure 1.** A typical structure of the fiber-reinforced bending actuator.

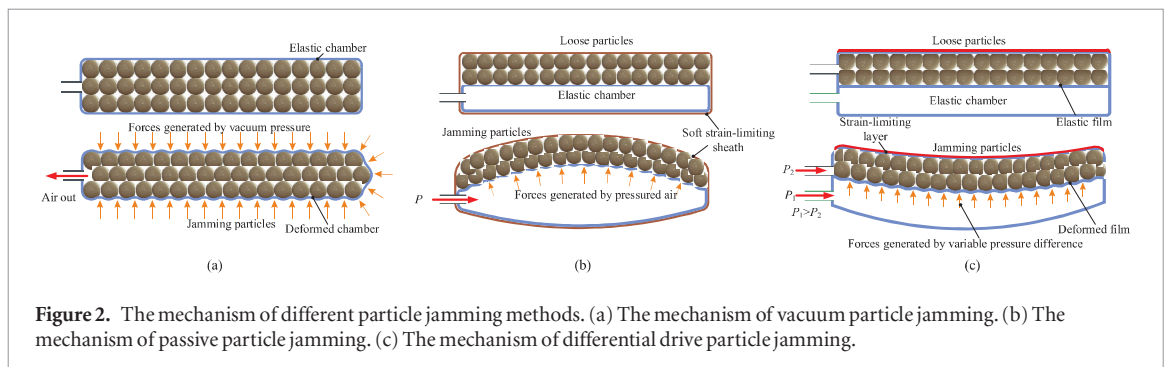


**Figure 2.** The mechanism of different particle jamming methods. (a) The mechanism of vacuum particle jamming. (b) The mechanism of passive particle jamming. (c) The mechanism of differential drive particle jamming.

fiber-reinforced bending actuator has a much simpler tubular geometry, which could simplify the process of the actuator design, and figure 1 demonstrates a typical structure of the fiber-reinforced bending actuator. The strain-limiting layer is integrated inside the actuator, which limits the bending direction of the actuator as the actuator is pressurized. Furthermore, the fiber reinforcement constrains the radical deformation of the actuator. Polygerinos *et al* proposed a model to analyse the bending behavior in free space and the interaction forces when in contact with the environment [13, 14]. The bending angle and the stiffness of the fiber-reinforced bending actuator depend on the pressure of the compressed air. However, the pressure range of the actuator is limited due to the elastomer material and the fabrication of the actuator. This drawback restricts the application of these actuators for heavy loads. How to enhance the ability to modulate the stiffness of the actuator to adapt to different application scenarios has become a main challenge for soft robots.

Trappe *et al* addressed that particle jamming possesses some promising properties in stiffness variation at the beginning of this century [15]. For the particle jamming mechanism, particles are first capsuled

loosely in a soft chamber and show amazing compliance. However, particles jam each other firmly under vacuum pressure. The increasing interaction forces between particles and the elastic chamber result in high stiffness, as shown in figure 2(a). In addition, a positive pressure universal gripper was reported in [16]. The gripper shows adaptability and conformability in grabbing objects with irregular shapes in low stiffness while presenting high stiffness to handle or manipulate heavy loads. Furthermore, the vacuum particle jamming method was exploited to design robotic hands with variable stiffness [17]. Based on the vacuum jamming mechanism, Kim *et al* proposed a layer jamming method, which utilized the friction between the layers to modulate the stiffness [18].

Several actuators that combined the vacuum jamming and the pneumatic structure were proposed in recent years [19–21]. These actuators usually have an air chamber and a particle chamber. In the grasping process, the vacuum pump is initially turned off, and the particles, which are in their natural state, are forced to conform to an object shape as the pneumatic compartment is pressurized. Then, the vacuum pump is turned on, jamming the particles inside the pack to

increase the stiffness. Note that directly vacuumizing the particle chamber in the deformation phase results in a large differential pressure between the two chambers, which will stiffen the actuator and resist further deformation of the actuator. Therefore, these dual-chamber actuators based on the vacuum jamming method cannot achieve deformation and stiffness variation simultaneously.

In addition to the vacuum-based jamming, researchers have proposed other methods of stiffness variation. Pettersson *et al* designed a universal gripper using magnetorheological (MR) fluids to realize passive shape adaptation. The stiffness variation is achieved by controlling an applied magnetic field. In this method, magnetic particles will be rearranged by applying an external electric or magnetic field. The force between particles caused by the field will make them squeeze together, which increases the stiffness of the actuator [22]. Soft actuators made of low melting point alloys (LMPAs) can also achieve variable stiffness since a large stiffness range can be achieved when LMPAs change between solid and liquid states. Furthermore, variable stiffness soft robots that used LMPAs have been developed [23–25] in recent years. Yang *et al* proposed a potential method for stiffness variation by using an acoustic-based method [26]. In this method, particles can be rearranged by acoustic waves, which can create the particle jamming effect to modify the stiffness.

Inspired by these particle jamming methods, Li *et al* proposed a passive particle jamming method [27], as shown in figure 2(b). A pack of particles is integrated on one side of an elastic chamber, and they are confined to a soft sheath. Once the chamber inflates, the particles will jam under the pressure of the chamber, and the stiffness increases. In vacuum jamming, the vacuum pressure between the outside and the inside of the particle pack results in an evenly distributed pressure to squeeze the particles, whereas in the passive jamming, the particle pack jams to increase the stiffness under an external force, which is due to the pressure on the membrane between the particle pack and the pneumatic chamber. However, the stiffness variation of the actuator is coupled with the bending motion, and the reacting force of the particle pack will restrict the actuator from further bending, which also limits the bending range of the passive particle jamming actuator. The inability to adjust the bending angle and the stiffness independently is the main drawback of the passive particle jamming method.

Motivated by the advantage of the passive particle jamming method, a variable stiffness actuator is proposed based on a dual-deformable chamber structure with one chamber filled with particles, and two chambers can be pressurized independently, which is shown in figure 2(c). In differential drive particle jamming, the air chamber is inflated with a higher pressure than the particle chamber. The inflation of the actuator causes a bending behavior due to the fiber rein-

forcement and the strain-limiting layer. Meanwhile, the pressure difference between the two chambers makes the particles jam each other, which increases the stiffness of the actuator. Compared with the actuator based on vacuum jamming, the actuator based on differential drive particle jamming can achieve simultaneous deformation and stiffness variation by differentially driving the two chambers, and freedom from the use of vacuum power is another advantage of the proposed actuator over an actuator based on vacuum jamming.

Importantly, the main contributions of this paper are as follows:

- (1) The differential drive particle jamming method is proposed as an effective way to adjust the stiffness of a soft actuator, which has not yet been reported in the literature.
- (2) A dual-chamber structure is proposed based on a differential drive particle jamming mechanism, which can independently control the bending angle and the stiffness simultaneously by adjusting the air pressure.
- (3) Theoretical models are presented to characterize the bending motion and stiffness variation of the actuator.

The paper is organized as follows. Section 2 demonstrates the basic actuator structure of the proposed gripper. In addition, several models are presented to characterize the bending motion and stiffness variation in section 3. Section 4 presents the fabrication process of the gripper based on the differential drive particle jamming method. The experimental performances of the gripper and the actuator are analyzed to verify the validity of the proposed models in section 5. Finally, section 6 concludes the paper.

## 2. Actuator design

To describe the bending behavior of the proposed gripper, the structure of the actuator is discussed first. Based on the widely used fiber-reinforced bending structure [28], a dual-deformable chamber actuator is proposed, which consists of an air chamber with a semicircular cross-section, a particle chamber filled with particles, a strain-limiting layer embedded beneath the particle chamber, and a fiber reinforcement layer winding in a double helix pattern around the two chambers, as shown in figure 3. The air chamber and the particle chamber are fabricated by hyperelastic material, and the two chambers can be actuated by pressurized air independently. Furthermore, the strain-limiting layer and the fiber reinforcement layer are fabricated using polyethylene cloth and nylon fiber, respectively.

Due to the inextensibility of the strain-limiting layer, simultaneous inflation of the two chambers can



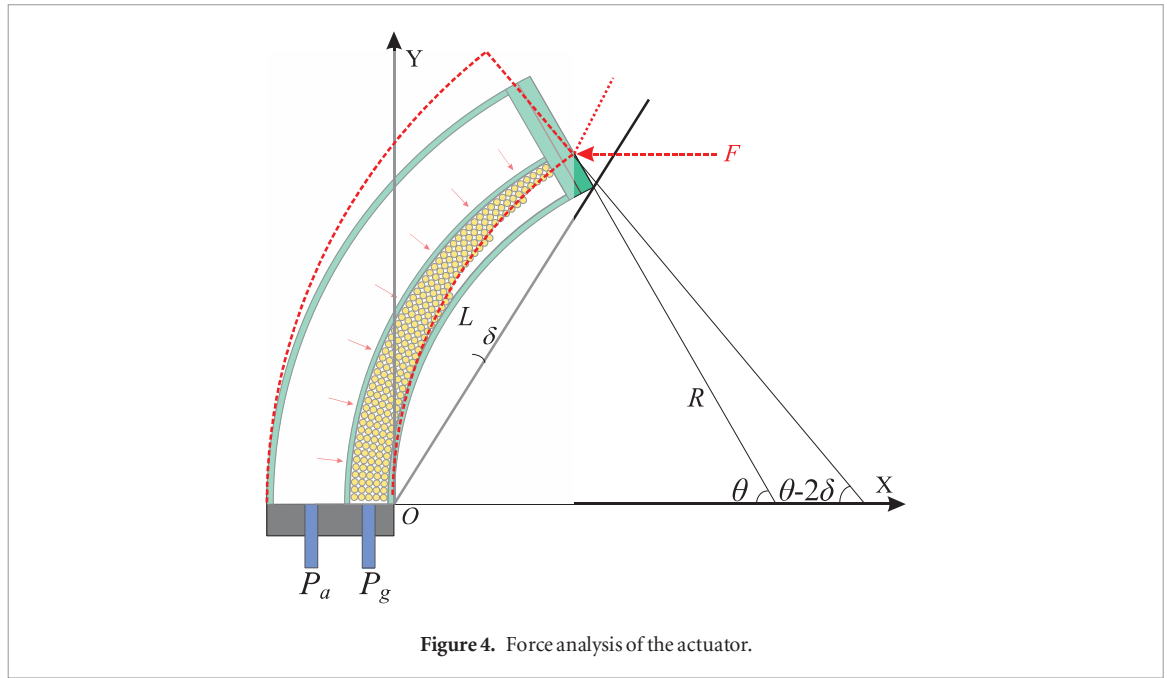


Figure 4. Force analysis of the actuator.

Since the fiber-reinforcement encircles the whole actuator, the bending effect due to the tension of the fiber-reinforcement is negligible. Therefore, a moment equilibrium around the original point  $O$  holds:

$$M_a = M_e + M_p, \quad (1)$$

where  $M_a$  is the bending moment of the internal air pressure against the actuator.

### 3.1.2. The moment of particle jamming

The moment due to particle jamming is caused by the friction between the particles and the inner surface of the particle chamber. When there is no compressional force applied on the particles, the particles can move freely and the actuator can bend easily. Nevertheless, if there is a differential pressure  $P_d = P_a - P_g$ , the compressing force increases the friction between the particles and the inner surface of the chamber, which restrains the particles from moving.

Referring to [30], the compressing force can be obtained through the analogy of the static liquid model based on Pascal's principle, as shown in figure 5. The differential pressure  $P_d$  applied to the particles is transmitted to every inner layer of the particle chamber without attenuation. The compressing forces on the inner layers of the chamber can be calculated by multiplying  $P_d$  and the equivalent area.

The friction  $f$  between the particles and the bottom layer of the particle chamber is tangent to the curvature of the actuator. To calculate the moment due to the friction on the bottom layer, an infinitesimal strip on the bottom layer of the particle chamber is defined as  $\Delta S$ , whose length and width are  $2r$  and  $(R + d_1)d\gamma$  respectively, and  $\gamma$  is the center angle, as shown in figure 6. In addition, the moment due to the friction on the bottom layer can be calculated as:

$$M_{p1} = \mu P_d \int_0^\theta 2r \left( \frac{L}{\theta} + d_1 \right)^2 \sin^2 \gamma - 2r \left( \frac{L}{\theta} + d_1 \right) \left( \frac{L}{\theta} - \left( \frac{L}{\theta} + d_1 \right) \cos \gamma \right) \cdot \cos \gamma d\gamma, \quad (2)$$

where  $\mu$  is the friction coefficient between the particles and the layer of the particle chamber.

Meanwhile, the moments generated by the frictions on the side layers and the upper layer of the particle chamber can also be formulated in the same way as:

$$M_{p2} = 2\mu P_d \int_0^\theta d_2 \left( \frac{L}{\theta} + d_1 + \frac{d_2}{2} \right)^2 \sin^2 \gamma - d_2 \left( \frac{L}{\theta} + d_1 + \frac{d_2}{2} \right) \left( \frac{L}{\theta} - \left( \frac{L}{\theta} + d_1 + \frac{d_2}{2} \right) \cos \gamma \right) \cos \gamma d\gamma, \quad (3)$$

$$M_{p3} = \mu P_d \int_0^\theta 2r \left( \frac{L}{\theta} + d_1 + d_2 \right)^2 \sin^2 \gamma - 2r \left( \frac{L}{\theta} + d_1 + d_2 \right) \left( \frac{L}{\theta} - \left( \frac{L}{\theta} + d_1 + d_2 \right) \cos \gamma \right) \cos \gamma d\gamma. \quad (4)$$

Consequently, the combined moments due to particle jamming can be formulated as:

$$M_p(\theta, P_d) = M_{p1} + M_{p2} + M_{p3}. \quad (5)$$

Note that  $d_1$ ,  $d_2$  and  $r$  are structural parameters of the particle chamber, and  $\mu$  is only correlated with the material of the particle. Therefore,  $M_p$  can be considered as a function of the bending angle and the differential pressure. Furthermore,  $M_p$  changes linearly with the differential pressure, which provides the possibility to change the stiffness dynamically by controlling the differential pressure.

### 3.1.3. The moment of air pressure

The moment of the air pressure consists of the bending moments due to the pressure on the



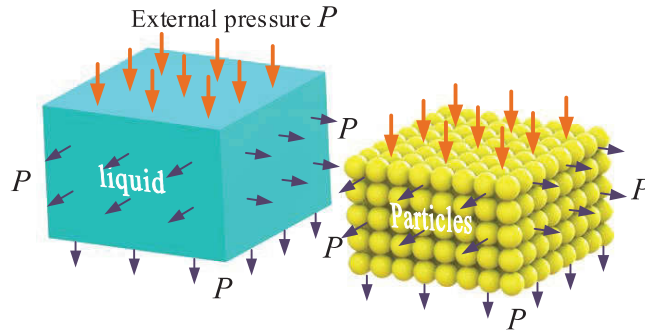


Figure 5. The transmission of the pressure between particles.

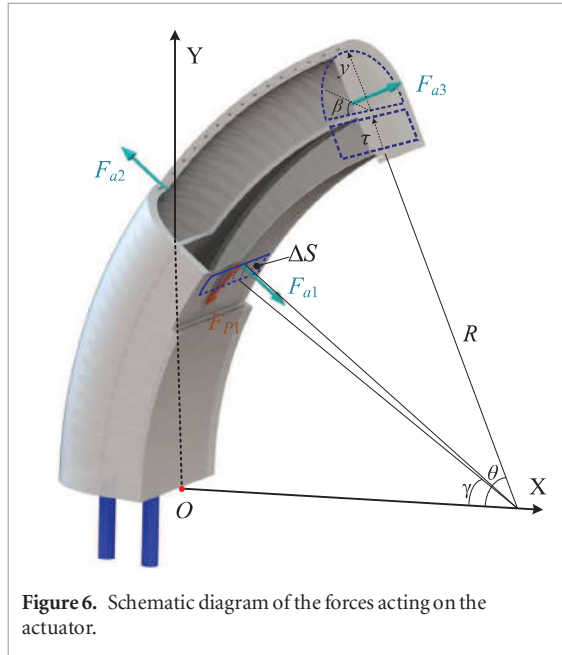


Figure 6. Schematic diagram of the forces acting on the actuator.

bottom rectangular layer, the top semicircular layer and the distal cap of the actuator, as shown in figure 6.

To analyze the moment due to the air pressure on the bottom rectangular layer, we first focus on the infinitesimal strip  $\Delta S$  on the bottom rectangular layer of the actuator, which is defined the same as before. Since the moment generated by the Y-component of the force is fairly small due to the short force arm, only the moment generated by the X-component of the force is formulated as follows:

$$M_{a1} = \int_0^\theta 2P_a r \left( \frac{L}{\theta} + d_1 \right)^2 \cos \gamma \sin \gamma d\gamma. \quad (6)$$

Note that the pressure of the particle chamber is  $P_g$ , but the differential pressure between two chambers will be transmitted to the layers of the particle chamber by the particles according to section 3.1.2. Namely, the combined effects of the pressure acting on the bottom rectangular layer are still  $P_a$ . This reveals that all the chambers are driven by the same pressure  $P_a$ , regardless of the chamber pressure  $P_g$ . Therefore, the air chamber pressure  $P_a$  can be considered as the driving pressure of the whole actuator.

By introducing the local coordinate  $\beta$ , as shown in figure 6, the moment of the top semicircular layer around point O can be formulated similarly as follows:

$$M_{a2} = - \int_0^\theta \int_0^\pi P_a r \left( \frac{L}{\theta} + d_1 + d_2 + d_3 + r \sin \beta \right)^2 \sin \beta \cos \gamma \sin \gamma d\gamma d\beta. \quad (7)$$

By introducing the local coordinates  $\gamma$  and  $\tau$ , shown in figure 6, the bending moment due to the air pressure on the distal cap of the actuator, which is denoted as  $M_{a3}$ , can be formulated as:

$$M_{a3} = 2 \int_0^r P_a \sqrt{r^2 - y^2} \left( (G_1 + y) \sin^2 \theta - \cos \theta \left( \frac{L}{\theta} - (G_1 + y) \cos \theta \right) \right) dy + \int_0^{d_2} 2r P_a \left( \left( \frac{L}{\theta} + d_1 + \tau \right) \sin^2 \theta - \cos \theta \left( \frac{L}{\theta} - \left( \frac{L}{\theta} + d_1 + \tau \right) \cdot \cos \theta \right) \right) d\tau, \quad (8)$$

where  $G_1 = L/\theta + d_1 + d_2 + d_3$ . Combining the effect of the pressurized air acting on the multiple layers of the actuator, the moment of the air pressure can be obtained as:

$$M_a(\theta, P_a) = M_{a1} + M_{a2} + M_{a3}. \quad (9)$$

According to (8) and (9), it can be found that in addition to the preset structure parameters (such as  $d_0$ ,  $d_1$ ,  $d_2$ ,  $d_3$  and  $r$ ),  $M_a$  is determined by the bending angle  $\theta$  and the air chamber pressure  $P_a$ .

#### 3.1.4. The moment of elastic stress

Silicone rubber is used to fabricate the proposed actuator, which can be considered as a homogeneous incompressible Neo-Hookean (NH) material [31]. According to [13], the radial stress vanishes, and the circumferential stress is significantly smaller than the axial stress; therefore, the axial stress is treated as the only nonvanishing principal stress in this paper, which is denoted as  $s$  in this study.

The moment due to combining the effect of the stresses consists of the moments of the internal stress in the top hemi-circular layer, the side layers, the inner

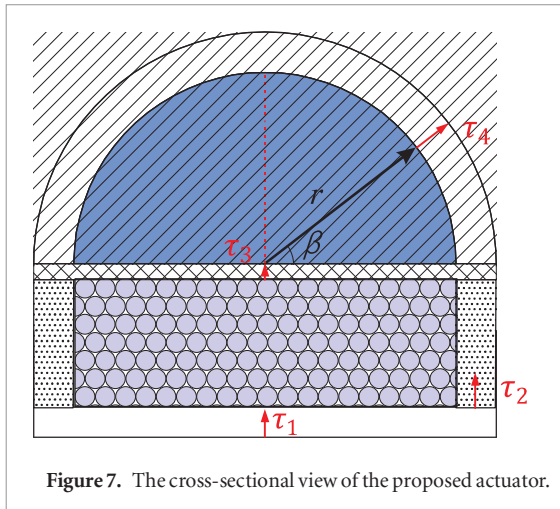


Figure 7. The cross-sectional view of the proposed actuator.

layer and the bottom layer. By introducing the local coordinates  $\tau_1$ ,  $\tau_2$ ,  $\tau_3$ ,  $\tau_4$  and  $\beta$ , shown in figure 7, the axial stretch of each part can be formulated as follows:

$$\lambda_{\tau_1} = \frac{R + \tau_1}{R} = \frac{L + \tau_1 \theta}{L}, \quad (10)$$

$$\lambda_{\tau_2} = \frac{R + d_1 + \tau_2}{R} = \frac{L + (d_1 + \tau_2) \theta}{L}, \quad (11)$$

$$\lambda_{\tau_3} = \frac{R + d_1 + d_2 + \tau_3}{R} = \frac{L + (d_1 + d_2 + \tau_3) \theta}{L}, \quad (12)$$

$$\lambda_{\tau_4} = \frac{R + d_1 + d_3 + d_2 + (r + \tau_4) \sin \beta}{R} = \frac{L + (d_1 + d_3 + d_2 + (r + \tau_4) \sin \beta) \theta}{L}, \quad (13)$$

where  $\lambda_{\tau_1}$ ,  $\lambda_{\tau_2}$ ,  $\lambda_{\tau_3}$  and  $\lambda_{\tau_4}$  are the axial stretch of the bottom layer, the side layers, the inner layer and the top hemi-circular layer, respectively. Thus, the corresponding stresses  $s_i$  ( $i = 1, \dots, 4$ ) can be calculated as follows:

$$s_i = c \left( \lambda_{\tau_i} - \frac{1}{\lambda_{\tau_i}^3} \right) \quad i = 1, \dots, 4, \quad (14)$$

where  $c$  is the initial shear modulus of the material. Combining the effect of the stresses acting on the actuator, the moment generated by the internal stretch around the point  $O$  can be calculated as:

$$\begin{aligned} M_e(\theta) = & \int_0^{d_1} s_1(2r + 2d_0)L\tau_1 d\tau_1 + 2 \int_0^{d_2} s_2 d_0(d_1 + \tau_2) \\ & \cdot L d\tau_2 + \int_0^{d_3} s_3(2r + 2d_0)L(d_1 + d_2 + \tau_3) d\tau_3 \\ & + \int_0^{d_0} \int_0^\pi s_4(d_1 + d_2 + d_3 + (r + \tau_4) \sin \beta) \\ & \cdot (r + \tau_4) L d\beta d\tau_4. \end{aligned} \quad (15)$$

### 3.1.5. Analytical model of bending angle

The moment equilibrium equation around the origin point  $O$  can be formulated as:

$$M_a(\theta, P_a) = M_e(\theta) + M_p(\theta, P_d). \quad (16)$$

Equation (16) is an equation of  $\theta$  on the condition that the design parameters, such as  $d_0$ ,  $d_1$ ,  $L$  and  $r$ , are given. Nevertheless, since the integral in (15) could not be computed analytically, (16) is a transcendental equation. Thus, there is no analytical solution for  $\theta$ , and the solution can only be obtained by numerical algorithms. Note that  $M_a$  is determined by the pressure of the air chamber and the bending angle, while  $M_p$  is a linear function of the differential pressure. If there is no differential pressure, i.e.  $M_p$  equals zero, the bending angle is only determined by the pressure of the air chamber, which is similar to the fiber-reinforced bending actuator. Furthermore, it also provides the possibility to decouple the bending angle control from the stiffness control.

### 3.2. Analysis of actuator's stiffness

Before modelling the stiffness of the actuator, the stiffness measurement method is defined first. In the stiffness measurement process, the actuator is applied with a certain air pressure to bend an initial angle  $\theta$ . Subsequently, an external force  $F$  is applied at the end-point of the actuator until the actuator restores a small rotational angle  $\delta$  around the origin  $O$  [32]. The stiffness of the proposed actuator, which refers to the rotational stiffness, is defined as:

$$k = \frac{M_f}{\delta}, \quad (17)$$

where  $M_f$  is the external moment, and  $\delta$  is the rotational angle due to the external moment. Since the centre of the circular arc formed by the actuator lies on the  $X$  axis, according to the geometric relationship shown in figure 4, the final bending angle is  $\theta - 2\delta$ . The final bending angle can be obtained based on the displacement of the actuator end-point. For experimental modelling, the external moment  $M_f$  can be calculated by  $M_f = FR \sin \theta$ .

To model the stiffness of the actuator theoretically, the moment equilibrium with the external moment is discussed first. At the free bending stage, the air pressure  $P_a$  leads to the free bending of the actuator towards the particle chamber, and the internal stretch of the hyperelastic material results in an opposing bending moment  $M_e$ . Once the external force  $F$  is applied on the actuator, correspondingly, the moment  $M_f$  generated by the external force  $F$  causes a reverse bending of the actuator. Meanwhile, the frictions between particles and the layer of the particle chamber cause a particle jamming torque  $M_p$ , which restrains further reverse bending of the actuator. Therefore, a moment equilibrium around the origin point  $O$  can be formulated as:

$$M_a + M_p = M_e + M_f. \quad (18)$$

The moments due to the air pressure, the particle jamming and the elastic stress can be formulated by (5), (9) and (15), respectively. Based on the definition of the stiffness, the stiffness of the actuator can be calculated as:

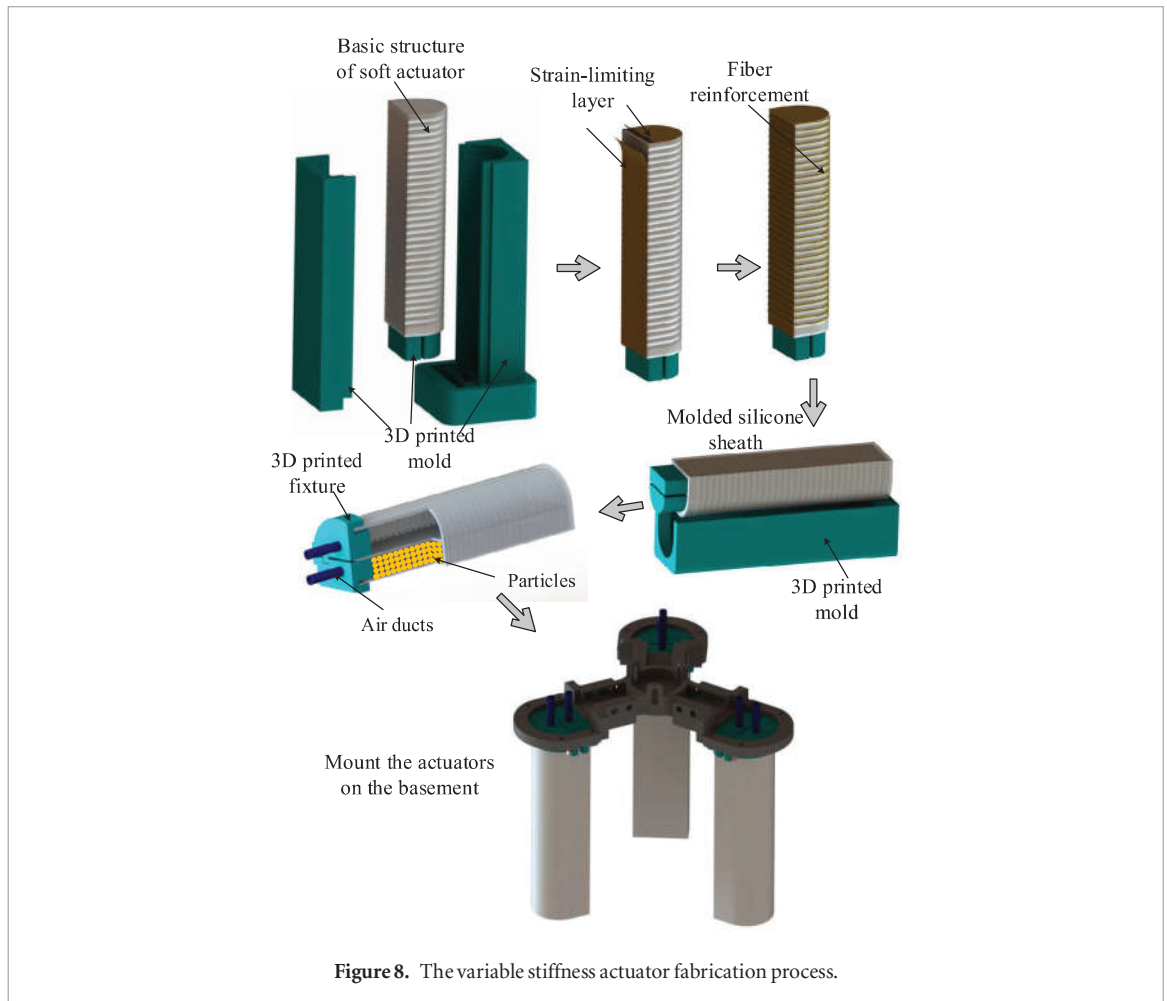


**Figure 8.** The variable stiffness actuator fabrication process.

$$k = \frac{M_a(\theta - 2\delta, P_a) + M_p(\theta - 2\delta, P_d) - M_e(\theta - 2\delta)}{\delta}. \quad (19)$$

According to (19), the stiffness can be formulated as a function of the initial bending angle  $\theta$  and the air pressure  $P_a$  and  $P_d$  on the condition that the design parameters are given. However,  $\theta$  can be eliminated using the solution of (16). Therefore, the stiffness can be determined only by the air pressure  $P_a$  and  $P_d$ . Similar to the previous discussion, the integral in (15) cannot be computed analytically, and the stiffness can only be solved numerically. According the bending angle model, it is found that the bending angle is mainly determined by the pressure of the air chamber. On the condition that the pressure of the air chamber is set,  $M_p$  can be increased by increasing the differential pressure of the two chambers, which can stiffen the actuator dynamically without affecting the bending angle.

#### 4. Gripper fabrication

A prototype of the proposed gripper has been fabricated to verify the validity of the model. The fingers and the base of the gripper were fabricated separately. The multistep moulding approach was adopted to fabricate the fingers, as shown in figure 8. Three-dimensional (3D)-printed

moulds with a hemi-circular rod and a rectangular rod were used to define the contour of the key dual-chamber structure of the actuator. Then, the silicone rubber cured inside these moulds. The silicone soft actuators were fabricated with silicone rubber EON-10, which was produced by Shenzhen Yi-Heng Fine Chemical Co., Ltd. In addition, polyethylene cloth was pasted on the bottom outside surface of the particle chamber as the strain-limiting layer, and the fiber was wound in a double helix pattern around the outside surface of the dual-chamber structure. A layer of silicone rubber was applied to encapsulate the whole assembly in another mould, which embedded the fiber reinforcement and the strain-limiting layer in the dual-chamber structure. The two rods were removed from the dual-chamber structure, and the open distal end was capped by placing it into uncured silicone. Then, corn particles were filled into the particle chamber, and after the distal end cured, the proximal end was sealed in the same way. Two vented ducts were mounted on the proximal end cap to connect the pressure air tubes to the chambers separately. Pressurized air can be fed to the actuator by an air pump through the air ducts, and two valves were used for the air pressure control. Finally, three fingers were fixed on the base fabricated by a 3D printer to complete the assembly process of the gripper, as shown in figure 8.



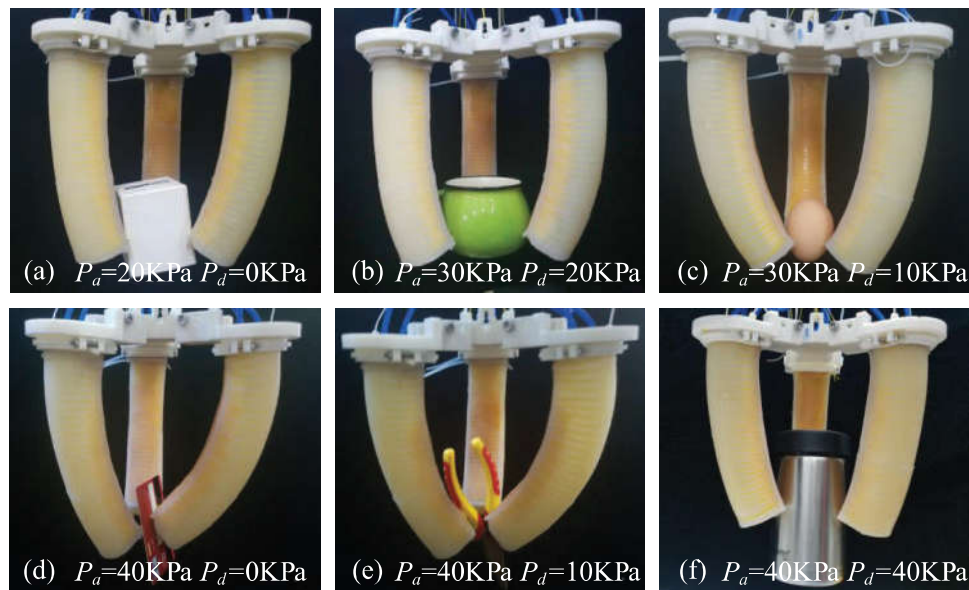


**Figure 9.** Demonstration of the proposed gripper's compliance and adaptiveness. (a) Grasp a cube. (b) Grasp a cup. (c) Grasp an egg. (d) Grasp a card. (e) Grasp a plier. (f) Grasp a bottle.

## 5. Experimental performance

### 5.1. Grasping object performance

#### 5.1.1. Tests of grasping of different objects

To verify the compliance and adaptiveness of the proposed gripper, objects of various shapes and materials were grasped by the proposed gripper. Figure 9 shows the grasping of a cube, a cup, an egg, a card, a plier and a bottle, which demonstrates the good adaptivity to irregular objects and the compliance for fragile objects. The process of grasping the experiments is shown in the supplementary video.

#### 5.1.2. Tests of load capacity

To measure the load capacity of the proposed gripper, the proposed gripper was used to grasp spherical shells filled with metal parts, which shows approximate maximum load capacity. In the load capacity test, the pressures of the air chamber and the particle chamber were set as the desired values to seize the spherical shell. Then, metal parts were gradually added into the spherical shell until the spherical shell began to slide, and the final weight was the load capacity of the proposed gripper under the specific pressure. The results are shown in figures 10(a)–(c), which reveal that the load capacity of the proposed gripper is improved as the driving pressure increases. The gripper based on the fiber-reinforced bending structure was also tested for comparison, and the actuator was designed with a similar structure to the proposed gripper except that there is no particle chamber, and the corresponding cross-section is also shown in figure 10. It can be found that the load capacity of the gripper based on the fiber-reinforced bending actuator is much smaller than that of the proposed gripper under the same air pressure. Note that the load capacity of the gripper based on the fiber-reinforced bending actuator reaches 479 g at a

driving air pressure of 60 KPa, while the load capacity of the proposed gripper can reach 1669 g at the same air pressure, which is over three times more than the other gripper.

### 5.2. Experiments of stiffness

To further verify the property of the gripper and the validity of the models proposed in section 3, several groups of experiments were conducted. The measurement platform, as shown in figure 11, was set up to measure the bending angle and stiffness of the actuator. The proposed actuator was mounted on the horizontal rail, while the force gauge was set on the vertical rail to measure the value of the external force; coordinate paper was used to record the position of the actuator's end-point in the bending process.

First, several groups of experiments were carried out to verify the stiffness of the proposed model. In the stiffness experiments, both chambers of the actuator were driven independently, and the actuator bent freely. Then, an external force was applied at the end-point of the actuator through the measuring head of the force gauge so that the actuator bent backwards  $\delta = 5^\circ$ . The force was measured by the force gauge, while the air pressures were recorded by the pressure gauges. The measurement processes were repeated 30 times to obtain the average value of  $P_a$ ,  $P_d$  and  $F$ .

#### 5.2.1. Analysis of stiffness modelling and experimental results

To verify the validity of the stiffness model proposed in section 3.2, an actuator with structure parameters  $d_0 = 4$  mm,  $d_1 = 4$  mm,  $d_2 = 12$  mm,  $d_3 = 1$  mm,  $r = 18$  mm and  $L = 144$  mm was driven by air pressure ranging from 0 to 60 KPa at an interval of 5 KPa, while the pressure differentials were set at four different values. The computed values of the stiffness

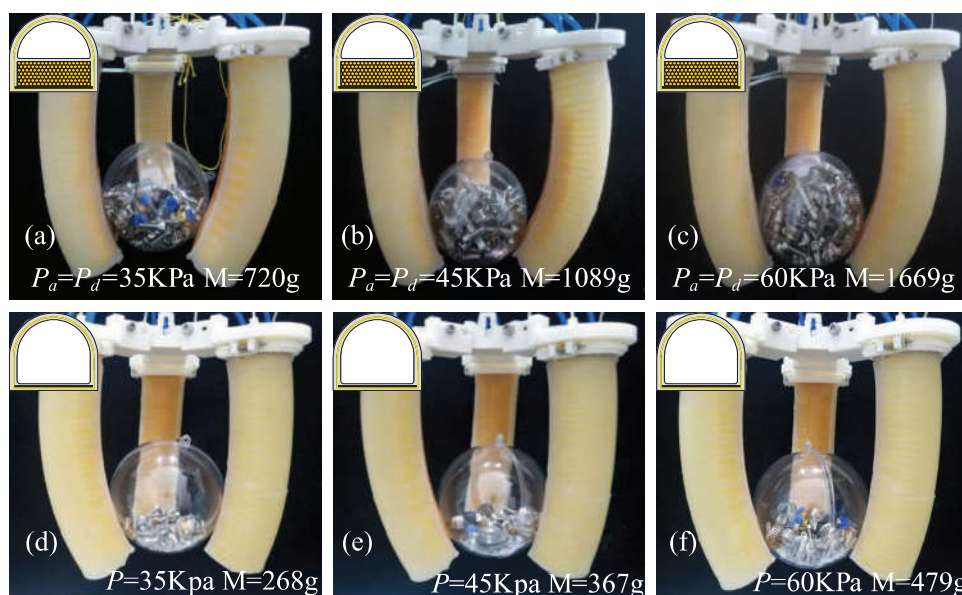


**Figure 10.** Load capacity comparisons of the proposed gripper and gripper based on the fiber-reinforced bending actuator. (a)–(c) The load capacity of proposed gripper at different pressures. (d)–(f) The load capacity of the gripper based on the fiber-reinforced bending actuator at different pressures.

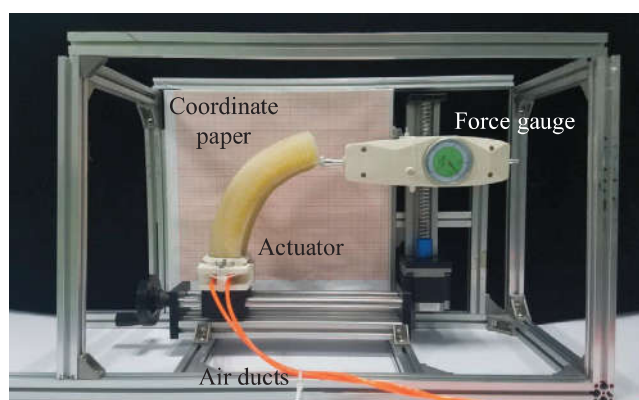


**Figure 11.** Experiment platform.

based on (19) are plotted as curves in black lines, while experimental data are plotted as red dots, as shown in figure 12.

The results demonstrate that the stiffness increases as the pressure increases, and the proposed stiffness model can effectively predict the stiffness variation as the pressure changes. Furthermore, the experimental results are slightly larger than the corresponding computational ones. This phenomenon may stem from two aspects: first, the tension of the strain-limiting layer is ignored, which contributes to the moment against the bending towards the particle chamber. This may directly affect the stiffness of the actuator. Second, the ability of particle jamming to convert the external pressure into the friction force seems to have a nonlinear property, namely, an upper threshold of the friction force due to particle jamming exists, so that the same rate of increase cannot be maintained as the differential pressure.

### 5.2.2. Influence of the air pressure

Equation (19) demonstrates that the stiffness is directly affected by the air chamber pressure and differential pressure. However, equation (19) does not have an analytical solution; therefore, a group of experiments were carried out to explore the relation between the stiffness and the air pressure explicitly, which is shown in figure 13.

The experimental results reveal that the stiffness increases smoothly as the air chamber pressure rises, if the differential pressure remains constant, as shown in figure 13. When the air chamber pressure is given, the increase in stiffness occurs nearly evenly as the differential pressure rises from 0 KPa to 20 KPa. This phenomenon can be explained by considering that the stiffness is mainly affected by the moment due to particle jamming that is based on the condition that the air chamber pressure remains at a constant value. According to section 3.1.2, the moment due to particle

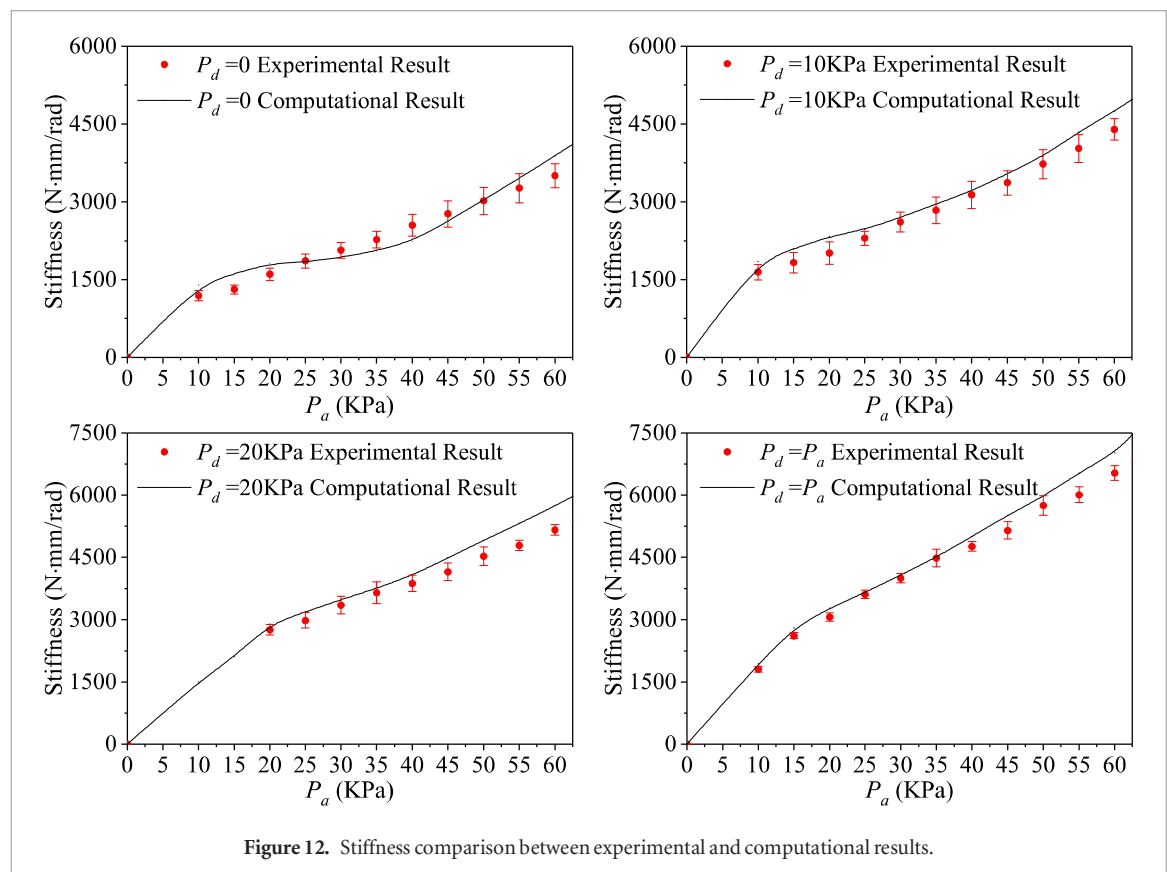


Figure 12. Stiffness comparison between experimental and computational results.

jamming is a linear function of the differential pressure, which results in the even increase of the stiffness with respect to the differential pressures. Note that the curve that corresponds to the case of  $P_a = P_d$  grows rapidly. The reason is that when  $P_a = P_d$ , the differential pressure changes dynamically with the air chamber pressure rather than remaining at a constant value. In addition, the region between the curve  $P_d = 0$  and the curve  $P_d = P_a$ , which are the minimum and maximum values of the differential pressure, respectively, is the range that is reachable for the actuator, which provides the possibility to control the stiffness of the actuator flexibly.

### 5.2.3. Influence of structure parameters

In addition to the air pressure, the design parameters of the actuator structure, such as the layer thickness  $d_0$ , also affects the stiffness of the actuator. To explore the stiffness variation in response to the design parameters, experiments using different actuators with layer thickness  $d_0 = 3$  mm,  $d_0 = 4$  mm and  $d_0 = 5$  mm were carried out, and the corresponding results are presented in figure 14. The results reveal that the value of the layer thickness will not change the trend that the stiffness increases as the pressure increases; however, there is an inverse correlation between the stiffness and the layer thickness of the actuator. This phenomenon can be explained as follows. If the layer thickness of the actuator increases, the corresponding principal stretch ratios and stresses will rise simultaneously according to section 3.1.4, which directly increases the moment of the elastic

stress; therefore, the stiffness decreases based on (19). It is worth noting that although smaller layer thickness can achieve an improvement in stiffness, a smaller layer thickness may increase the difficulty of the actuator fabrication as well.

### 5.2.4. Influence of particles

Since the particles are another design parameter that affect the stiffness of the actuator, a group of experiments were carried out to explore the influence of the particles filled in the actuator. Corn particles, desiccant particles (calcium chloride) and plastic spherical particles were sealed into the actuator, and the layer thickness was set  $d_0 = d_1 = 4$  mm, while the other parameters were set the same as before. In this experiment, the air chamber pressure  $P_a$  rose from 0 to 60 KPa, while  $P_d = P_a$  to guarantee that the actuator maintained the completely jamming state in the expansion process. Additionally, the experimental results are shown in figure 15.

Compared to the actuator without particles, it can be found that the particles can improve the stiffness of the actuator significantly. Under the same pressure, the stiffness of the actuator with plastic spherical particles is smaller than the actuator with corn particles or desiccant particles. The reason is that the friction coefficient of plastic spheres is much smaller due to the smooth surface and the regular spherical shape, which directly reduces the moment of the particle jamming; therefore, the stiffness of the corresponding actuator is smaller than that of the other two. The surface roughness of desiccant particle is similar to that

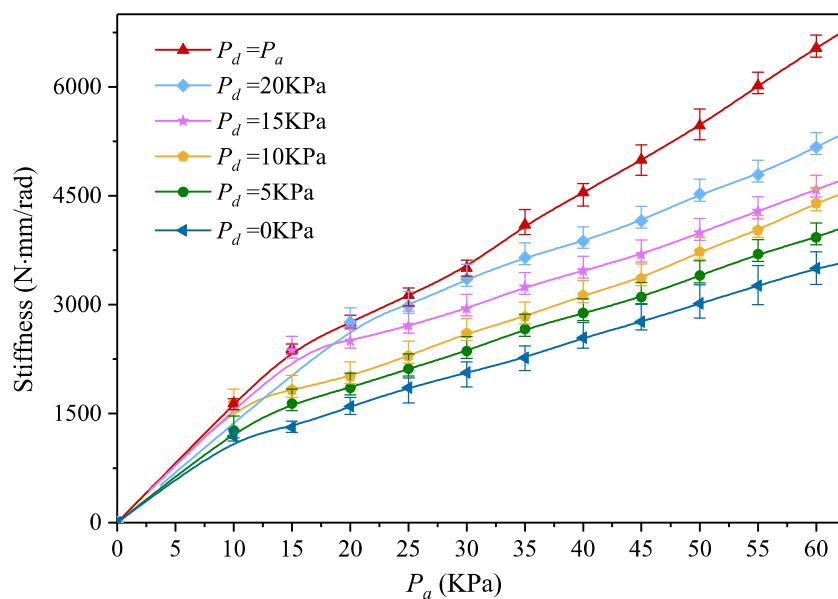


Figure 13. The relationship between the stiffness and the air pressure.

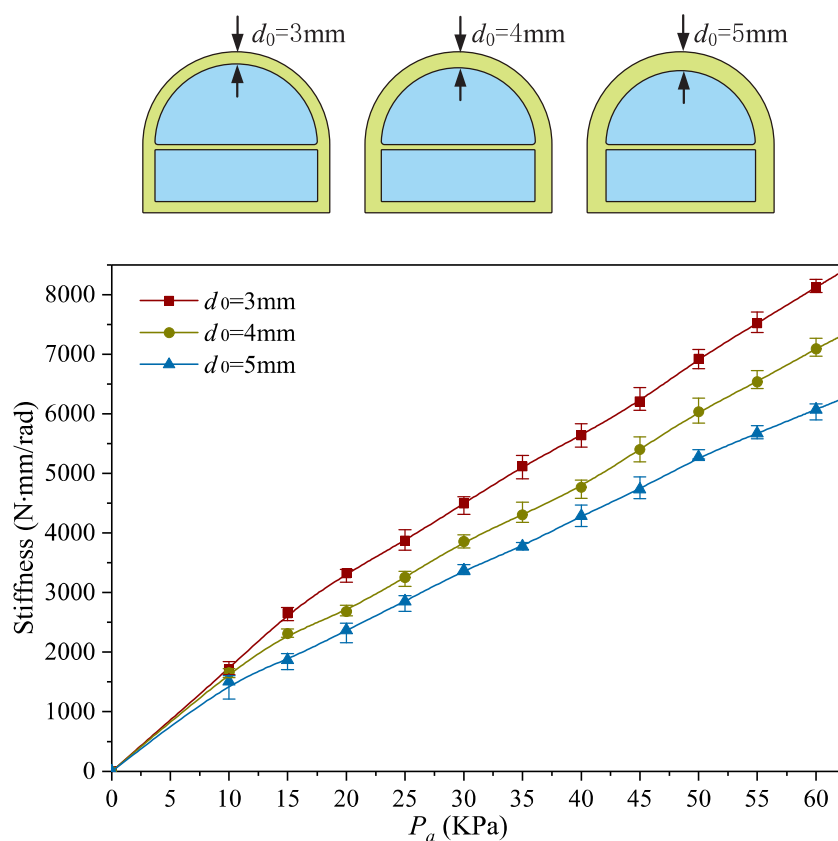


Figure 14. The relationship between the stiffness and the layer thickness of the actuator.

of corn particles, but the diameter is larger than that of corn particles. Generally, the particle chamber can be more fully filled with particles of small sizes, and the higher filling density of the space causes a positive effect on the stiffness of the actuator. Thus, the stiffness of the actuator filled with desiccant particles is between that of the corn and the plastic particles. Note that the stiffness curve of the actuator with corn parti-

cles is not very smooth compared to the other actuators. The phenomenon can be explained by considering that the corn particles show a poor fluidity when they are squeezed under pressure due to their rough surfaces and irregular shapes. Consequently, the nonuniform distribution of corn particles might occur in each expansion process, which results in the unsmooth stiffness curve.

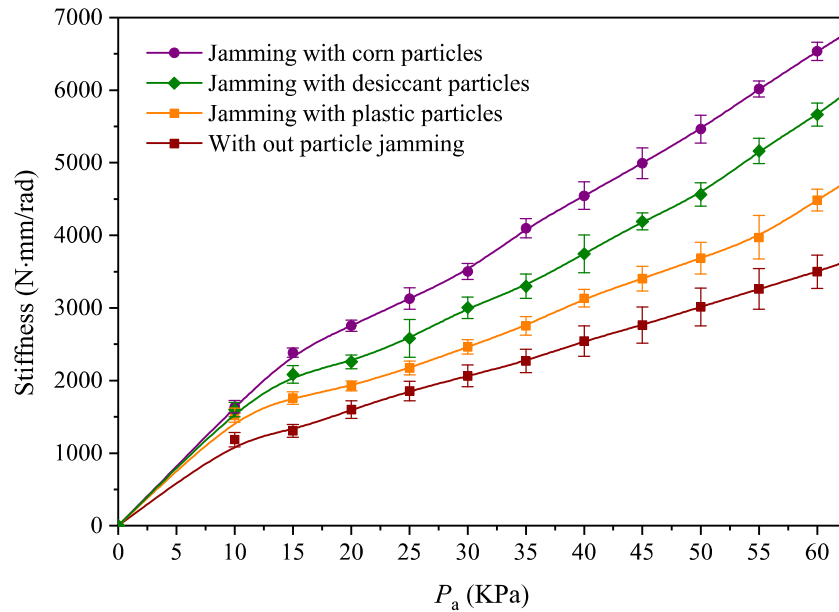


Figure 15. Influence of different filled particles.

### 5.3. Experiments of bending angles

In this section, experiments were carried out to verify the validity of the proposed bending angle modelling method. The layer thickness was set to  $d_0 = d_1 = 4$  mm, the other structure parameters were set the same as before, and the corn particles were sealed into the particle chamber. The computational values of the bending angle can be obtained by solving equation (16) with numerical algorithms, which are plotted as curves, while experimental data are plotted as dots, as shown in figure 16.

The experiment results show that the bending angle of the actuator increases significantly as the air chamber pressure increases, while the bending angle under the full particle jamming state ( $P_a = P_d$ ) is slightly smaller than the one without particle jamming ( $P_d = 0$ ). This phenomenon can be explained by the larger pressure difference between the two chambers that strengthens the squeezing effect between the particles and the chamber layers; thus, the moment due to particle jamming increases, which restricts further bending of the actuator. Note that the experimental results are in general smaller than the corresponding computational ones. The discrepancies may be caused by the linearization of the NH model at large deformations [14]. Furthermore, the tension in the strain-limiting layer is ignored during the modelling process. Due to these reasons, the computational results of the bending angle have some discrepancies with the experimental results.

### 5.4. Comparison with other soft bending actuators

To verify the efficacy of the proposed method, several experiments based on the fiber-reinforced bending actuator and the passive jamming actuator proposed by Li *et al* [27] were carried out for comparison. The bending angles and the stiffness of the actuators were measured and are plotted in figure 17. The green area

represents the reachable range of the bending angle and the stiffness of the proposed actuator, while the purple line and the dark blue line represent the reachable ranges of the passive jamming actuator and the fiber-reinforced bending actuator, respectively. In addition, figure 17 demonstrates two advantages of the proposed actuator:

- (1) A wider reachable range of the stiffness and bending angle. Figure 17 reveals that the bending angle of the fiber-reinforced bending actuator can vary in the range of  $[0, 70]$  degrees, and the stiffness will rise slightly due to the increase of the air pressure. In addition, the passive jamming actuator can increase its stiffness significantly as the bending angle rises up to 53 degree. However, the high stiffness restricts the further bending of the actuator. The proposed actuator can achieve a wide range of bending by controlling the differential pressure and air chamber pressure properly. The stiffness and bending angle of the fiber-reinforced bending actuator and the passive jamming actuator are confined on the purple line and the dark blue line, respectively, while the stiffness and bending angle of the proposed actuator can vary in the whole green region, which provides much more potential for the application where both high stiffness and high dexterity are required.
- (2) Decoupling of the stiffness and the bending angle. Both the passive jamming actuator and the fiber-reinforced bending actuator can achieve the stiffness variation as the air pressure increases. For the two actuators, the stiffness and the bending angle vary



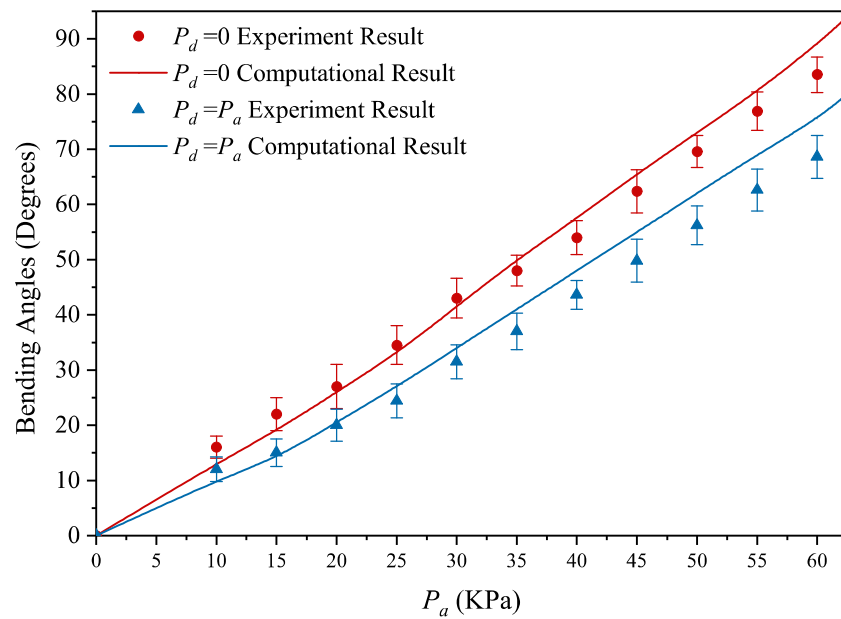


Figure 16. The bending angle comparison between experimental and computational results.

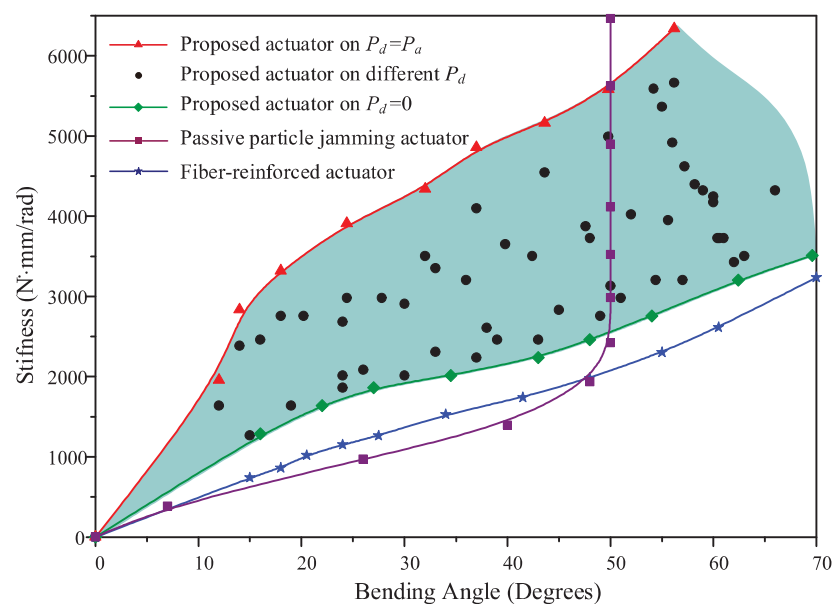


Figure 17. The stiffness and bending angle characteristics of the pneumatic actuators.

synchronously as the air pressure increases; thereby, the stiffness is coupled with the bending angle, and given that the mapping relationship of the stiffness and bending angle is an inherent characteristic of the corresponding actuator, it is impossible to regulate the stiffness and the bending angle independently. However, the proposed actuator can regulate the stiffness and the bending angle independently by adjusting the differential pressure and the air chamber pressure, namely, the proposed actuator achieves the decoupling of the stiffness and the bending angle, which provides the ease of the actuator's control.

## 6. Conclusion

The soft gripper is endowed with a fantastic adaptability and flexibility in grasping irregularly shaped and fragile objects. However, the low stiffness of the soft actuator limits the range of applications. To achieve stiffness variation, this study proposed a novel differential drive particle jamming mechanism that is capable of independent control of the stiffness and the bending angle, which is unlike previous research using the vacuum particle jamming or the passive particle jamming method. The soft actuator based on the differential drive particle jamming mechanism is characterized by a dual-deformable chamber structure with one chamber filled with particles. The decoupled

control of the stiffness and the bending angle can be achieved by properly adjusting the differential pressure and the air chamber pressure.

Theoretical models were developed to quantify the relationships between the pressures in two chambers, the design parameters, the bending angle and the stiffness. Furthermore, a gripper was fabricated to verify the validity of the analytical models. The experimental results have shown that the analytical model can estimate the stiffness and the bending angle with good accuracy, and has advantages in a wider reachable range of the stiffness and bending angle.

## Acknowledgment

This work was supported in part by the National Natural Science Foundation of China under Grant 51705050, Grant 51709023, and in part by the Technology Innovation and Application Demonstration Project of Chongqing under Grant cstc2018jszx-cyzdx0110.

## ORCID iDs

Pei Jiang  <https://orcid.org/0000-0003-3471-4151>  
Michael Z Q Chen  <https://orcid.org/0000-0001-7922-8371>

## References

- [1] Gaiser I et al 2008 A new anthropomorphic robotic hand *Humanoids IEEE-RAS Int. Conf. on Humanoid Robots* (IEEE) pp 418–22
- [2] Paez L, Agarwal G and Paik J 2016 Design and analysis of a soft pneumatic actuator with origami shell reinforcement *Soft Robot.* **3** 109–19
- [3] Kim H-S, Lee J-Y, Chu W-S and Ahn S-H 2017 Design and fabrication of soft morphing ray propulsor: undulator and oscillator *Soft Robot.* **4** 49–60
- [4] In H, Kang B B, Sin M and Cho K-J 2015 Exo-glove: a wearable robot for the hand with a soft tendon routing system *IEEE Robot. Autom. Mag.* **22** 97–105
- [5] Vikas V, Cohen E, Grassi R, Sozer C and Trimmer B 2016 Design and locomotion control of a soft robot using friction manipulation and motor-tendon actuation *IEEE Trans. Robot.* **32** 949–59
- [6] Zhang T S, Kim A, Ochoa M and Ziaie B 2015 Controllable somersaultmagnetic soft robotics *28th IEEE Int. Conf. on Micro Electro Mechanical Systems* (IEEE) pp 1044–7
- [7] Li T, Keplinger C, Baumgartner R, Bauer S, Yang W and Suo Z 2013 Giant voltage-induced deformation in dielectric elastomers near the verge of snap-through instability *J. Mech. Phys. Solids* **61** 611–28
- [8] Wehner M, Truby R L, Fitzgerald D J, Mosadegh B, Whitesides G M, Lewis J A and Wood R J 2016 An integrated design and fabrication strategy for entirely soft, autonomous robots *Nature* **536** 451
- [9] Nakamura T, Saga N and Yaegashi K 2003 Development of a pneumatic artificial muscle based on biomechanical characteristics *IEEE Int. Conf. on Industrial Technology* vol 2 (IEEE) pp 729–34
- [10] Mosadegh B, Polygerinos P, Keplinger C, Wennstedt S, Shepherd R F, Gupta U, Shim J, Bertoldi K, Walsh C J and Whitesides G M 2014 Pneumatic networks for soft robotics that actuate rapidly *Adv. Funct. Mater.* **24** 2163–70
- [11] Bishop-Moser J, Krishnan G, Kim C and Kota S 2012 Design of soft robotic actuators using fluid-filled fiber-reinforced elastomeric enclosures in parallel combinations *IEEE/RSJ Int. Conf. on Intelligent Robots and Systems* (IEEE) pp 4264–9
- [12] Galloway K C, Polygerinos P, Walsh C J and Wood R J 2013 Mechanically programmable bend radius for fiber-reinforced soft actuators *16th Int. Conf. on Advanced Robotics* (IEEE) pp 1–6
- [13] Polygerinos P, Wang Z, Overvelde J T B, Galloway K C, Wood R J, Bertoldi K and Walsh C J 2015 Modeling of soft fiber-reinforced bending actuators *IEEE Trans. Robot.* **31** 778–89
- [14] Wang Z, Polygerinos P, Overvelde J T B, Galloway K C, Bertoldi K and Walsh C J 2017 Interaction forces of soft fiber reinforced bending actuators *IEEE/ASME Trans. Mechatronics* **22** 717–27
- [15] Trappe V, Prasad V, Cipelletti L, Segre P N and Weitz D A 2001 Jamming phase diagram for attractive particles *Nature* **411** 772
- [16] Amend J R, Brown E, Rodenberg N, Jaeger H M and Lipson H 2012 A positive pressure universal gripper based on the jamming of granular material *IEEE Trans. Robot.* **28** 341–50
- [17] Jiang A, Xynogalas G, Dasgupta P, Althoefer K and Nanayakkara T 2012 Design of a variable stiffness flexible manipulator with composite granular jamming and membrane coupling *IEEE/RSJ Int. Conf. on Intelligent Robots and Systems* (IEEE) pp 2922–7
- [18] Kim Y-J, Cheng S, Kim S and Iagnemma K 2013 A novel layer jamming mechanism with tunable stiffness capability for minimally invasive surgery *IEEE Trans. Robot.* **29** 1031–42
- [19] Wall V, Deimel R and Brock O 2015 Selective stiffening of soft actuators based on jamming *IEEE Int. Conf. on Robotics and Automation* (IEEE) pp 252–7
- [20] Wei Y, Chen Y, Ren T, Chen Q, Yan C, Yang Y and Li Y 2016 A novel, variable stiffness robotic gripper based on integrated soft actuating and particle jamming *Soft Robot.* **3** 134–43
- [21] Hongliang Y, Fengyu X, Yudong Y and Pengfei Z 2017 Design and analysis of variable stiffness soft manipulator based on jamming structure *IEEE Int. Conf. on Robotics and Biomimetics* pp 657–62
- [22] Pettersson A, Davis S, Gray J O, Dodd T J and Ohlsson T 2010 Design of a magnetorheological robot gripper for handling of delicate food products with varying shapes *J. Food Eng.* **98** 332–8
- [23] Schubert B E and Floreano D 2013 Variable stiffness material based on rigid low-melting-point-alloy microstructures embedded in soft poly (dimethylsiloxane) (pdms) *RSC Adv.* **3** 24671–9
- [24] Shintake J, Schubert B, Rosset S, Shea H and Floreano D 2015 Variable stiffness actuator for soft robotics using dielectric elastomer and low-melting-point alloy *IEEE/RSJ Int. Conf. on Intelligent Robots and Systems* (IEEE) pp 1097–102
- [25] Nakai H, Kuniyoshi Y, Inaba M and Inoue H 2002 Metamorphic robot made of low melting point alloy *IEEE/RSJ Int. Conf. on Intelligent Robots and Systems* vol 2 (IEEE) pp 2025–30
- [26] Yang Y, Li Y and Chen Y 2018 Principles and methods for stiffness modulation in soft robot design and development *Bio-Des. Manuf.* **1** 14–25
- [27] Li Y, Chen Y, Yang Y and Wei Y 2017 Passive particle jamming and its stiffening of soft robotic grippers *IEEE Trans. Robot.* **33** 446–55
- [28] Connolly F, Walsh C J and Bertoldi K 2017 Automatic design of fiber-reinforced soft actuators for trajectory matching *Proc. Natl Acad. Sci.* **114** 51–6
- [29] Maeder-York P, Clites T, Boggs E, Neff R, Polygerinos P, Holland D, Stirling L, Galloway K, Wee C and Walsh C 2014 Biologically inspired soft robot for thumb rehabilitation *J. Med. Devices* **8** 020933
- [30] Wei Y, Chen Y, Yang Y and Li Y 2016 A soft robotic spine with tunable stiffness based on integrated ball joint and particle jamming *Mechatronics* **33** 84–92
- [31] Ogden R W 1997 *Non-Linear Elastic Deformations* (New York: Dover)
- [32] Li Y, Chen Y and Li Y 2018 Distributed design of passive particle jamming based soft grippers *IEEE Int. Conf. on Soft Robotics (RoboSoft)* (IEEE) pp 547–52